Quantifying Tufa Growth Rates (TGRs) using Structure-from-Motion (SfM) Photogrammetry

Ivan Marić[1][a], Ante Šiljeg[1][b], Neven Cukrov[2][c] and Fran Domazetović[1][d]

[1]University of Zadar, Department of Geography, Trg kneza Višeslava 9, 23 000 Zadar, Croatia
[2]Ruđer Bošković Institute, Department of Marine and Environmental Research, Bijenička 54, Zagreb, Croatia

Keywords: Tufa Growth Rate (TGR), Structure from Motion (SfM), Digital Surface Model (DSM).

Abstract: The production of high-quality digital surface models (DSMs) is an increasing interest throughout the various geomorphometry studies. Consequently, a wide range of advanced geospatial methods has been used at different scales. Despite the fact that Structure-from-Motion (SfM) photogrammetry is one of the most popular methods until now it has not been systematically applied in the studies of tufa formation dynamics (TFD). In this paper, we propose a framework for using SfM photogrammetry and GIS tools in the measurement of tufa growth rates (TGRs). TGRs were measured on two limestone plates (PLs) within the area of Roški waterfall in Croatia. Four submillimetre resolution DSMs of tufa have been created. TGR was 0.407 mm for a six-month period. Checkpoints were used to calculate errors. The results confirm the efficiency of the SfM at this scale. Research shows that photogrammetric measurement system design can produce extremely dense point clouds with high horizontal and vertical accuracy. The application of SfM and GIS in the measurement of TFD can be the great methodological improvement for specific geomorphometric applications at smaller scales.

1 INTRODUCTION

Advances in geomatics have revolutionized the ability to quantitatively record the Earth's surface (Doulamis et al., 2015, Aucelli et al., 2016, Smith et al., 2016). Consequently, a wide range of modern geospatial devices has been used at different scales (Šiljeg et al., 2019, Verma and Bourke 2019). Despite that, the most popular device for measurement of tufa formation dynamics (TFD) is still modified micro-erosion meter (MEM) (Arenas et al., 2014, Arenas et al., 2010, Drysdale and Gillieson, 1997), a mechanical device which has numerous drawbacks of which the most prominent are: compaction problem, false erosion occurrence, large measurement error (Drysdale and Gillieson, 1997) and small sampling density. To our knowledge, modern geospatial technologies, such as high-quality hand-held laser scanning devices and 3D projection scanners, have not yet been used in the process of TFD measurement.

Only, Marić et al. (2019) indicated the possibility of using SfM photogrammetry in the measurement of TFD.

SfM is a relatively low cost, widely used method in the creation of 2.5 and 3D models (Verma and Bourke 2019, Smith et al., 2016). It uses overlapping digital images taken from different positions to produce a 3D point cloud (Verma and Bourke 2019). SfM is based on a bundle adjustment (BA) algorithm which uses image metadata and automated scale-invariant feature transform (SIFT) image matching method to estimate 3-D geometry and camera positions (Smith et al., 2016). The recent advances in SfM have yet to be widely applied to micro-scale landforms (Verma and Bourke 2019).

Tufa is terrestrial highly porous monomineral rock typical for karst areas (Capezzuoli, 2014) formed in freshwaters of ambient to near ambient temperature (Carthew et al., 2003). The formation of tufa is highly localized (Pevalek, 1965). Research

---

[a] https://orcid.org/0000-0002-9723-6778
[b] https://orcid.org/0000-0001-6332-174X
[c] https://orcid.org/0000-0003-3920-6703
[d] https://orcid.org/0000-0003-3920-6703

about tufa tends to quantify tufa growth (TGR) and erosion rates. Precise measurement of the rates is important for several reasons. Firstly, it addresses the basic geomorphological question of the single landscape element genesis and evolution. Secondly, differences in rates may indicate specific changes in the environment (Liu et al., 2011, Liu, 2017). Rates can be expressed as the height of the tufa formed or eroded per time (eg. mm a^{-1}) or as the mass accumulated or lost per unit area at some time (eg. mg cm^2 a^{-1}). They were calculated by various direct and indirect methods. Direct methods are more reliable because they refer to the physical measurement of formed precipitate (Gradziński, 2010). They can include micro-erosion meter (MEM) (Arenas et al., 2014, Arenas et al., 2010, Drysdale and Gillieson, 1997), mass increments (Liu, 2017, Gradziński, 2010, Pentecost and Coletta, 2007), accretion pins (Statham, 1977), vernier caliper (Baker and Smart, 1995) and scanning electron microscope (SEM) (Tran et. al., 2019). In general, there are very few studies that examined linear (mm a^{-1}) or volumetric (mm^3 a^{-1}) rates over long-term intervals (Demott et al., 2019).

In this research, an SfM measurement workflow for determination of TGRs is presented on the case study of Roški waterfall at the National park "Krka" (NPK) in Croatia. Two main objectives were: propose a framework for using SfM photogrammetry in GIS measurement of TGRs and determine the average TGR for the wider area of Roški waterfall.

2 STUDY AREA

TGRs were monitored at the study area of Roški waterfall within NPK in Croatia (Figure 1). NPK is located in the Šibenik-Knin County between 43°47'036" and 44°03'218" N and 15°55'894" and 16°09'919" E. NPK is one of the youngest National parks in Croatia with the main purpose of preserving the natural and cultural heritage of the Krka River. The climate of the NPK has characteristics of moderately warm Mediterranean rainy climate (Köppen classification Csa) with dry and hot periods in summer. Rainfall is highest in the cold part of the year, from October to February.
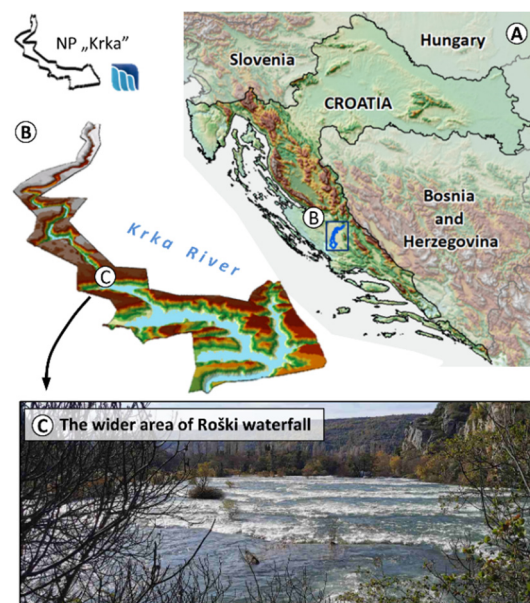

Figure 1: A) Location of Croatia B) NPK and C) and wider area of the Roški Waterfall.

3 MATERIALS AND METHODS

3.1 Installation of PLs

TGRs were measured on the upper surface (16 cm²) of the limestone plate (PL). The upper surface of the PLs should not be reflective and texturally homogeneous because this may cause an error in the automatic feature-matching process (Micheletti et al., 2015). The PLs were positioned at a location in the immediate surroundings of the Roški waterfall (Figure 2). A unique ID and name were assigned to a location, while a code was engraved beneath each PL.
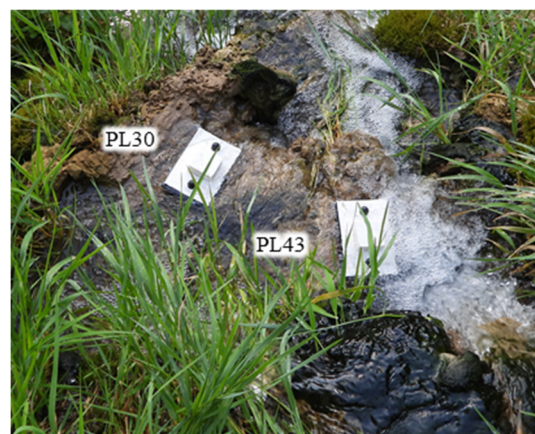

Figure 2: PLs positioned near Roški waterfall.

Each PL was measured before being put in flow. PLs were fixed with two stainless steel screws on July 1st, 2019. They were left drying at room temperature for 4 days, before the second measurement.

3.2 Photogrammetric Measurement System Design

The measurements of the PLs need to be done in such a way to minimize the common problems that occur in a very close-range photogrammetry process. They include uneven light intensity, shadow occurrences, shallow depth of field (DoF), blurred photos and insufficient photo overlap. These measurements can be called photogrammetric expert measurement systems (Ergun and Baz 2006). This process can be divided into five basic parts:

a) Device design;
b) Camera calibration;
c) Image acquisition;
d) Image workflow process;
e) Analysis of the measurements.

3.2.1 Device Design

Our device consisted of six parts. The first part is the pedestal on which an adjustable metal frame with fixed holders and rails for the movement of the frame are mounted. That frame moves along X, Y and Z axes. Horizontal movement determines the overlap between images while the vertical enabled adjustment of DoF. Image footprint and spatial resolution of the model are calculated by knowing the distance of the DSLR sensor from the local coordinate system (LCS) and the internal geometry of the DSLR.

The main component of the device is LCS. LCS is essential if high-quality 2.5D or 3D photogrammetric models want to be used in the measurement of the TFD. It can be created in several ways depending on the expertise of the operator, desired model accuracy, research purposes, and available equipment. LCS are mostly created using coded targets (markers) which are reference points for coordinate system and scale definition (Verma and Bourke, 2019, Tushev et al., 2017). Coordinates of targets can be determined by different techniques: total station (Skarlatos et al., 2019), using a precise coordinatograph with high accuracy (Barilar et al., 2015), DSM (Direct Survey Method) (Balletti et al., 2015), etc.

In this research, LCS was created in CorelDRAW 2017 and screen-printed with a high-quality print technique that generates sharp and clear lines. The LCS is movable and placed in the four slots on the pedestal. In the middle of LCS, there is an opening through which surface of the PL peaks above the LCS reference plane. The location and height of LCS above the pedestal must be set on the same value for every measurement. PL is then mounted on a pedestal by the adjustable metal frame and two fixed holders. PL always needs to be positioned at the same coordinates in LCS because that allows interval measurement of specific cross-sections. On the movable mechanical frame sensor system is mounted. The sensor system may consist of a suitable DSLR camera and a specific type of lens. Sensor system characteristics must be considered in detail when selecting the appropriate camera and lens type for specific 3D reconstruction purposes (Mosbrucker et al., 2017).

3.2.2 Camera Calibration

Accurate camera calibration is the essential component of photogrammetric measurement and the precondition for the 3D high-quality metrics extraction (Clarke and Fryer 1998). One of the most popular methods is self-calibration in which no calibration object exists and metric properties of the camera are determined from "non-calibration" photographs (Remondino and Fraser, 2006). In this research, camera calibration was performed by Agisoft Lens, the free part of the commercial Agisoft package, which has an implemented chessboard point detection algorithm. It calibrates the camera by standard bundle block adjustment algorithm. Determined intrinsic calibration parameters in *Agisoft Metashape 1.5.1* were fixed during the whole image workflow process.

3.2.3 Image Acquisition

Image acquisition is described as a "delicate step in (an) otherwise automated" photogrammetry workflow (Micheletti et al., 2015). It is necessary that all areas of interest need to be in ≥3 photographs (James and Robson, 2012). The horizontal movement of the mechanical frame enabled the determination of the front and side overlap between adjacent images. Image acquisition of PLs was performed in a 1:2 scale with Nikon D5300 on which macro lens Venus LAOWA 60mm f/2.8 was mounted. The sensor system on a mechanical frame was moved over PLs in a Double Grid Mission with a front and side overlap >80%. Each sample on the PL was recorded at more than 9 overlapping images. In one recording 187 overlapping images were acquired. This is important because, in general, a higher number of quality images improves better model quality and

produces denser point clouds and meshes (Micheletti et al., 2015). The sensor system was positioned 23.4 cm above the LCS. That removes the possibility of the large jump in image scale which produces different texture and makes it difficult to accurately match image features (Smith et al., 2016). The aperture was set on f/22. Although aperture within the range f/5.6 – f/11 produces the sharpest and the cleanest images (Hoiberg, 2018) this value was selected because it generates the biggest DoF. With this, we wanted to achieve a sharp image of the highest precipitated tufa sample on the PL and equally sharp image of the LCS located at the base of the plate. However, accurate determination of the desired DoF is difficult given the large variability of tufa growth rates worldwide (Viles and Pentecost 2007). The small aperture reduced the amount of incident light. This problem was solved a using ring flash that produced uniform illumination and removed shadows over the entire PL surface. The intensity of light within the image footprint was maintained on the constant level using the UT380 luminometer. ISO was set on 200 and shutter speed at 1/20. The focus of the lens and camera setting were fixed throughout the whole image acquisition process.

3.2.4 Image Workflow Process

Image workflow process was done in *Agisoft Metashape Professional 1.5.1* low-cost commercial 3D reconstruction software from Agisoft LLC, Russia (Rahaman and Champion, 2019). The saleable character of software limits detailed knowledge of the integrated algorithms (Stylianidis and Georgopoulos 2017). Camera calibration was loaded and fixed during the process. Marker accuracy parameter is set at 0 value because it's real value is within 0.02 m (Agisoft, 2019). In total image workflow process consisted of 10 steps which included:

(1) Image Quality Estimation
(Images with a quality value smaller than 0.5 are excluded from photogrammetric processing)
(2) Align Photos
(Accuracy settings were set on *High* because Metashape uses full resolution images. Key point and tie point limit were set on 0).
(3) Camera Calibration Parameters Fixed
(4) Iterative Application of Gradual Selection – Optimize Camera Location)
   1. Reprojection Error > 0.4
      Reconstruction Uncertainty > 60
      Projection Accuracy > 30

   2. Reprojection Error > 0.3
      Reconstruction Uncertainty > 50
      Projection Accuracy > 20
   3. Reprojection Error > 0.1
      Reconstruction Uncertainty > 30
      Projection Accuracy > 10
(5) Build Dense Cloud (DC) – Build Mesh (M)
Quality of Dense Cloud: Medium (DC)
Depth Filtering: Aggressive (DC)
Source Data: Dense Cloud (M)
Surface Type: Arbitrary (M)
Face Count: Medium (M)
(6) Add GCP and CP – Model Update
The orientation of the model in LCS was achieved by adding four ground control points (GCP). The accuracy was tested using four checkpoints (CP) (Figure 3) as a quality measure (Eltner et al., 2016). Ideal evaluation of the geometric quality of an SfM model should include more CPs that should be evenly distributed across the whole area of recording (Sanz-Ablanedo et al., 2018). However, in this case, the CPs could not be set on the whole recording scene because on it tufa is formed during interval measurements (Figure 3). The marking and measurement of the CPs on the tufa surface is not possible without the without the risk of being damaged. Therefore, the accuracy was tested with four checkpoints surrounding the PL (Figure 3).
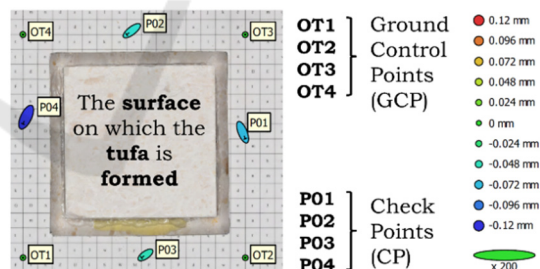

Figure 3: PLs positioned near Roški waterfall.

(7) Optimize Camera Location – Gradual Selection Tools
   1. Reprojection Error > 0.1
      Reconstruction Uncertainty > 30
      Projection Accuracy > 10
(8) Build DC – Build M – Build Texture (T)
Quality of Dense Cloud: High (DC)
Depth Filtering: Aggressive (DC)
Source Data: Dense Cloud (M)
Surface Type: Arbitrary (M)
Face Count: High (M)
Mapping Mode: Generic (T)

Texture Size: 4096 (T)

(9) Build Digital Elevation Model (DEM) – Build Orthomosaic (DOP)

DEM was generated from DC because it provides more accurate results. Interpolation mode was enabled. Build DEM uses the Inverse Distance Weighting (IDW) interpolation method. The selected surface for orthomosaic generation process was DEM.

(10) Export Models

3.2.5 Calculation of TGRs using GIS

The TGR per PL was calculated as the height difference between the average height of all pixels on the measuring surface (16 cm²) from the final (6 months) and initial digital tufa high-resolution surface models (Figure 4). The average height of all pixels on the measuring surface was calculated using the *Raster Calculator* tool.
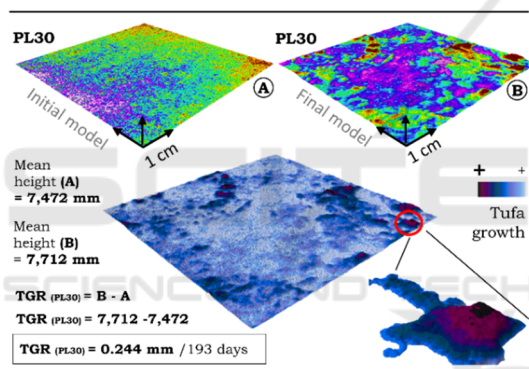

Figure 4: An example of tufa growth rate (TGR) calculation.

4 RESULTS AND DISCUSSION

4.1 Assessment of Measurement Quality

Root Mean Square Error (RMSE), Standard Deviation (SD) and Mean Absolute Deviation (MAD) were used as surface quality metrics (Table 1). They were calculated for four checkpoints on four different models (n=16). Errors for individual points (P_n) are calculated as a difference between the source (X, Y and Z value derived from LCS) and estimated values (X, Y and Z value derived from a created model). The difference between the control and checkpoints is in fact that control points are used for referencing/optimization procedures and checkpoints

aren't (Pasumansky, 2015). RMSE in referent coordinate system was 0.017 for X, 0.016 for Y and 0.091 mm for Z coordinate. Total RMSE was 0.094 mm and 0.251 pix. in the image coordinate system. MAD was 0.016 for X, 0.014 for Y and 0.083 mm for Z coordinate. Total MAD was 0.088 mm (Table 1). Total SD (0.034 mm) was smaller than RMSE and MAD. This indicates that measurement errors (the difference between the source and estimated values) are not too scattered around the mean (no outliers).

Table 1: Quality assessment of SfM measurement.

INITIAL STATE					
PL30	X (mm)	Y (mm)	Z (mm)	Total (mm)	Image (pix.)
P01	0.009	-0.022	-0.073	0.077	0.069
P02	-0.017	-0.013	-0.055	0.059	0.085
P03	-0.014	-0.009	-0.047	0.050	0.097
P04	-0.011	-0.023	-0.118	0.121	0.076
PL43	X (mm)	Y (mm)	Z (mm)	Total (mm)	Image (pix.)
P01	0.007	-0.017	-0.039	0.043	0.299
P02	-0.019	-0.004	-0.001	0.020	0.260
P03	-0.018	-0.010	0.081	0.084	0.650
P04	-0.015	-0.023	0.112	0.116	0.272
FINAL STATE					
PL30	X (mm)	Y (mm)	Z (mm)	Total (mm)	Image (pix.)
P01	0.014	-0.019	-0.047	0.053	0.130
P02	-0.016	-0.005	-0.139	0.140	0.180
P03	-0.015	-0.014	-0.117	0.119	0.166
P04	-0.027	-0.018	-0.096	0.102	0.135
PL43	X (mm)	Y (mm)	Z (mm)	Total (mm)	Image (pix.)
P01	0.018	-0.018	-0.110	0.113	0.256
P02	-0.017	-0.004	-0.112	0.113	0.226
P03	-0.015	-0.011	-0.092	0.094	0.283
P04	-0.021	-0.017	-0.095	0.099	0.193
RMSE	0.017	0.016	0.091	0.094	0.251
SD	0.014	0.007	0.071	0.034	0.141
MAD	0.016	0.014	0.083	0.088	0.211

The results show that the accuracy and precision of the LCS are submillimetre (<0.1 mm). The larger error for the Z-axis is not surprising, given the fact that there are more user-defined parameters that can potentially magnify the error. Checkpoints are within the DoF and the total displacement error is similar to reported values (Gajski et al., 2016, Marziali and Dionisio, 2017).

4.2 TGRs in Roški Waterfall Sedimentary System

The PLs were removed from the flow after six months (January 10th, 2020). They spent a total of 193 days in the water (Figure 5).
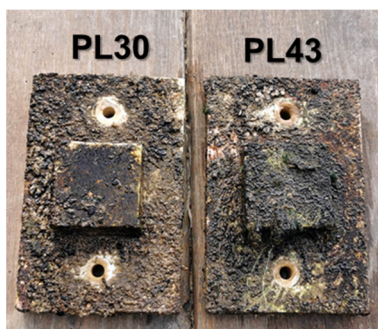

Figure 5: Surface of PLs after removal from the flow.

In total four very-high resolution digital surface models (Figure 6c-d) and digital orthophoto (DOP) of tufa (Figure 6a-b) were generated from which two represent initial PL shape and others shape after six months in the flow. TGRs were calculated based on three mil. samples on the 16 cm² area. The sampling density can be higher and lower. It is ultimately conditioned by the selected camera settings during the image acquisition and image processing workflow. In this case density was 188 898 samples per cm². In comparison, MEM generates around 0.15 samples per cm² (Drysdale and Gillieson, 1997).
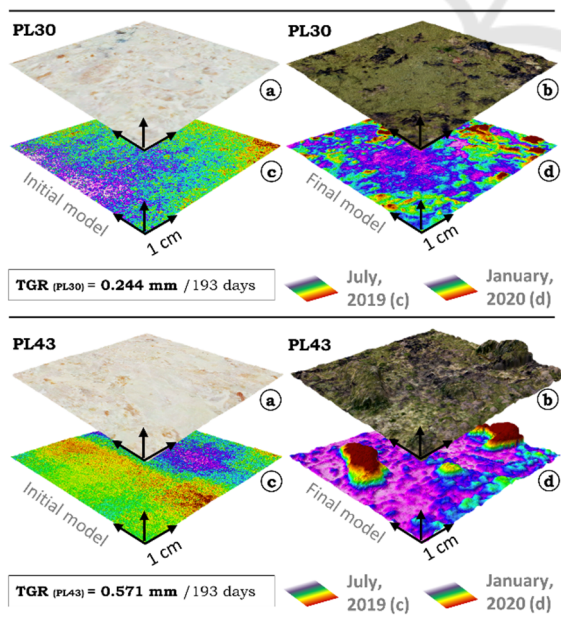

Figure 6: TGRs in the Roški waterfall.

During the six-month period (193 days) of the exposure to the flow, on the PL30 TGR was 0.244 and on the PL43 was 0.571 mm. The mean TGR for the specific location was 0.407 mm. The data obtained show that the tufa grew 2,101 μm per day.

5 CONCLUSION

Our approach uses high-resolution and quality digital images combined with the SfM workflow for TGR measurement. It provides an alternative and user-friendly method for the studying of TFD. This approach enables pre-design of image capturing plan, ensures high overlapping coverage of recording scene, static scene (PL), constant light conditions, avoids blurred images, allows the user to determine the spatial resolution of the model, DoF, and front and side overlap.

Submillimeter models generated by this method enable the derivation of specific morphometric parameters of complex tufa surface. Accurate and precise determination of growth and erosion rates with this approach will aid in the interpretation of the complex interrelationship between fluvial depositional subenvironments, physicochemical parameters of water and tufa fabric. A better understanding of the multi-scale tufa formation system could be achieved using this approach.

ACKNOWLEDGEMENTS

REFERENCES

Agisoft, 2019: Agisoft PhotoScan - Tips and Tricks, available at: http://www.agisoft.ru/w/index.php?title= PhotoScan/Tips_and_Tricks

Arenas C, Osácar C, Sancho C, Vázquez-Urbez M, Auqué L, Pardo G. 2010. Seasonal record from recent fluvial tufa deposits (Monasterio de Piedra, NE Spain): sedimentological and stable isotope data. *Geological Society, London, Special Publications* 336(1): 119-142.

Arenas C, Vázquez-Urbez M, Auqué L, Sancho C, Osácar C, Pardo G. 2014. Intrinsic and extrinsic controls of spatial and temporal variations in modern fluvial tufa sedimentation: A thirteen-year record from a semi-arid environment. *Sedimentology* 61(1): 90-132.

Aucelli, P. P., Conforti, M., Della Seta, M., Del Monte, M.,

D'uva, L., Rosskopf, C. M., Vergari, F. 2016. Multi‑temporal digital photogrammetric analysis for quantitative assessment of soil erosion rates in the Landola catchment of the Upper Orcia Valley (Tuscany, Italy). *Land Degradation & Development*, 27(4), 1075-1092.

Baker A, Smart PL. 1995. Recent flowstone growth rates: Field measurements in comparison to theoretical predictions. *Chemical Geology* 122(1-4): 121-128.

Barilar, M., Todić, F., Krste, I. (2015). Korištenje fotogrametrijskog materijala u izradi 3D modela i fototeksture. *Ekscentar*, (18), 50-56.

Balletti, C., Beltrame, C., Costa, E., Guerra, F., Vernier, P. (2015). Underwater Photogrammetry and 3D Reconstruction of Marble Cargos Shipwreck. International Archives of the Photogrammetry, Remote Sensing & Spatial Information Sciences.

Capezzuoli E, Gandin A, Pedley M. 2014. Decoding tufa and travertine (fresh water carbonates) in the sedimentary record: the state of the art. *Sedimentology* 61(1): 1-21.

Carthew KD, Taylor MP, Drysdale RN. 2002. Aquatic insect larval constructions in tropical freshwater limestone deposits (tufa): preservation of depositional environments. *General and Applied Entomology: the Journal of the Entomological Society of New South Wales* 31: 35 – 41.

Clarke, T. A., Fryer, J. G. (1998). The development of camera calibration methods and models. *The Photogrammetric Record*, 16(91), 51-66.

Demott LM, Scholz CA, Junium CK. 2019. 8200-year growth history of a Lahontan-age lacustrine tufa deposit. *Sedimentology* 66: 2169–2190.

Drysdale, R., & Gillieson, D. (1997). Micro-erosion meter measurements of travertine deposition rates: a case study from Louie Creek, Northwest Queensland, Australia. Earth Surface Processes and Landforms: *The Journal of the British Geomorphological Group*, 22(11), 1037-1051.

Doulamis, A., Soile, S., Doulamis, N., Chrisouli, C., Grammalidis, N., Dimitropoulos, K., ... Ioannidis, C. 2015. Selective 4D modelling framework for spatial-temporal land information management system. In Third International Conference on Remote Sensing and Geoinformation of the Environment (RSCy2015) (Vol. 9535, p. 953506). *International Society for Optics and Photonics*.

Eltner A, Kaiser A, Castillo C, Rock G, Neugirg F, Abellán A. 2016. Image-based surface reconstruction in geomorphometry–merits, limits and developments. *Earth Surface Dynamics* 4(2): 359-389.

Ergun, B., & Baz, I. (2006). Design of an expert measurement system for close-range photogrammetric applications. *Optical Engineering*, 45(5), 053604.

Gajski D, Solter A, Gašparović M. 2016. Applications of macro photogrammetry in archaeology. *Proceedings of the XXIII ISPRS Congress. Prague, Czech Republic*.

Gradziński M. 2010. Factors controlling growth of modern tufa: results of a field experiment. *Geological Society, London, Special Publications* 336(1): 143-191.

Hoiberg, C. (2018). The Best Aperture for Landscape Photography, retrieved at https://petapixel.com/2018/06/15/the-best-aperture-for-landscape-photography/

James, M.R., and Robson, S., 2012, Straightforward reconstruction of 3D surfaces and topography with a camera: accuracy and geoscience application: *Journal of Geophysical Research*, v. 117, 17 p.,

Liu L. 2017. Factors Affecting Tufa Degradation in Jiuzhaigou National Nature Reserve, Sichuan, China. *Water* 9(9): 702.

Liu Z, Sun H, Li H, Wan N. 2011. δ13C, δ18O and deposition rate of tufa in Xiangshui River, SW China: implications for land-cover change caused by climate and human impact during the late Holocene. *Geological Society, London, Special Publications* 352(1): 85-96.

Marić, I., Šiljeg, A., Cukrov, N., Roland, V., Goreta, G. (2019, June). 3D image based modelling of small tufa samples using macro lens in digital very close range photogrammetry. In *5th Jubilee International Scientific Conference GEOBALCANICA 2019*.

Marziali S, Dionisio G. 2017. Photogrammetry and macro photography. The experience of the MUSINT II Project in the 3D digitizing process of small size archaeological artifacts. *Studies in Digital Heritage* 1(2): 298-309.

Micheletti, N., Chandler, J.H., and Lane, S.N., 2015b, Structure from Motion (SfM) Photogrammetry: British Society of Geomorphology, *Geomorphological Techniques*, ch. 2, sec. 2.2, 12 p.

Mosbrucker, A. R., Major, J. J., Spicer, K. R., Pitlick, J. (2017). Camera system considerations for geomorphic applications of SfM photogrammetry. *Earth Surface Processes and Landforms*, 42(6), 969-986.

Pasumansky, A. 2015. Agisoft Forum, Topic GCP errors, Agisoft Technical Support, Available at: https://www.agisoft.com/forum/index.php?topic=2687.0, 9 March, 2020.

Pentecost A, Coletta P. 2007. The role of photosynthesis and CO2 evasion in travertine formation: a quantitative investigation at an important travertine-depositing hot spring, Le Zitelle, Lazio, Italy. J*ournal of the Geological Society* 164(4): 843-853.

Pevalek, I. (1956). Slap Plive u Jajcu na samrti. *Naše starine III*, 269-273.

Rahaman, H., Champion, E. 2019. To 3D or Not 3D: Choosing a Photogrammetry Workflow for Cultural Heritage Groups. *Heritage*, 2(3), 1835-1851.

Remondino, F., Fraser, C. (2006). Digital camera calibration methods: considerations and comparisons. International Archives of Photogrammetry, *Remote Sensing and Spatial Information Sciences*, 36(5), 266-272.

Sanz-Ablanedo, E., Chandler, J. H., Rodríguez-Pérez, J. R., Ordóñez, C. 2018. Accuracy of unmanned aerial vehicle (UAV) and SfM photogrammetry survey as a function of the number and location of ground control points used. *Remote Sensing*, 10(10), 1606.

Skarlatos, D., Menna, F., Nocerino, E., & Agrafiotis, P. (2019). Precision Potential of Underwater Networks for Archaeological Excavation Through Trilateration and Photogrammetry. *International Archives of the*

Photogrammetry, Remote Sensing and Spatial Information Sciences, 42(2/W10), 175-180.

Smith, M. W., Carrivick, J. L., Quincey, D. J. (2016). Structure from motion photogrammetry in physical geography. *Progress in Physical Geography*, 40(2), 247-275.

Statham I. 1977. 'A note on tufa-depositing springs in Glenasmole, Co. Dublin'. *Irish Geographer* 10: 14–18.

Stylianidis, E., Georgopoulos, A. 2017. Digital surveying in cultural heritage: the image-based recording and documentation approaches. In *Handbook of Research on Emerging Technologies for Digital Preservation and Information Modeling (pp. 119-149). IGI Global.*

Šiljeg, A., Barada, M., Marić, I., Roland, V. 2019. The effect of user-defined parameters on DTM accuracy—development of a hybrid model. *Applied Geomatics*, 11(1), 81-96.

Tran H, Rott E, Sanders D. 2019. Exploring the niche of a highly effective biocalcifier: calcification of the eukaryotic microalga Oocardium stratum Nägeli 1849 in a spring stream of the Eastern Alps. *Facies* 65(3): 37.

Tushev, S., Sukhovilov, B., Sartasov, E. (2017, October): Architecture of industrial close-range photogrammetric system with multi-functional coded targets. In *2017 2nd International Ural Conference on Measurements (UralCon)* (pp. 435-442). *IEEE*.

Verma, A. K., Bourke, M. C. (2019). A method based on structure-from-motion photogrammetry to generate sub-millimetre-resolution digital elevation models for investigating rock breakdown features. *Earth Surface Dynamics*, 7(1), 45-66.

Viles, H, Pentecost, A. (2007). Tufa and travertine. In DJ. Nash, SJ. McLaren (Esd.). Geochemical Sediments and Landscapes. (pp. 173-199). *Singapore: Blackwell Publishing Ltd*.